International Journal of Minerals, Metallurgy and Materials
Volume 29, Number 5, May 2022, Page 1120
https://doi.org/10.1007/s12613-022-2443-2

Self-supporting and hierarchically porous Ni_xFe–$S/NiFe_2O_4$ heterostructure as a bifunctional electrocatalyst for fluctuating overall water splitting

Wenjing Yan[1)], *Jintao Zhang*[1)], *Aijing Lü*[1)], *Songle Lu*[1)], *Yiwei Zhong*[1),✉], *and Mingyong Wang*[1,2),✉]

1) State Key Laboratory of Advanced Metallurgy, University of Science and Technology Beijing, Beijing 100083, China
2) Beijing Key Laboratory of Green Recovery and Extraction of Rare and Precious Metals, University of Science and Technology Beijing, Beijing 100083, China
(Received: 11 December 2021; revised: 28 January 2022; accepted: 21 February 2022)

Abstract: Stable non-noble metal bifunctional electrocatalysts are one of the challenges to the fluctuating overall water splitting driven by renewable energy. Herein, a novel self-supporting hierarchically porous Ni_xFe–$S/NiFe_2O_4$ heterostructure as bifunctional electrocatalyst was constructed based on porous Ni–Fe electrodeposition on three-dimensional (3D) carbon fiber cloth, *in situ* oxidation, and chemical sulfuration. Results showed that the Ni_xFe–$S/NiFe_2O_4$ heterostructure with a large specific surface area exhibits good bifunctional activity and stability for both hydrogen evolution reaction (HER) and oxygen evolution reaction (OER) because of the abundance of active sites, synergistic effect of the heterostructure, superhydrophilic surface, and stable, self-supporting structure. The results further confirmed that the Ni_xFe–S phase in the heterostructure is transformed into metal oxides/hydroxides and Ni_3S_2 during OER. Compared with the commercial 20wt% Pt/C||IrO_2–Ta_2O_5 electrolyzer, the self-supporting $Ni_{1/5}Fe$–$S/NiFe_2O_4$||$Ni_{1/2}Fe$–$S/NiFe_2O_4$ electrolyzer exhibits better stability and lower cell voltage in the fluctuating current density range of 10–500 mA/cm^2. Particularly, the cell voltage of $Ni_{1/5}Fe$–$S/NiFe_2O_4$||$Ni_{1/2}Fe$–$S/NiFe_2O_4$ is only approximately 3.91 V at an industrial current density of 500 mA/cm^2, which is lower than that of the 20wt% Pt/C||IrO_2–Ta_2O_5 electrolyzer (i.e., approximately 4.79 V). This work provides a promising strategy to develop excellent bifunctional electrocatalysts for fluctuating overall water splitting.

Keywords: self-supporting; hierarchically porous structure; heterostructure; bifunctional catalyst; overall water splitting

1. Introduction

Hydrogen production by water electrolysis has advantages in carbon emission, efficiency, and sustainability and is a promising method to solve the energy crisis and global climate change [1–2]. However, the water decomposition reaction is hindered by the slow kinetics of the hydrogen evolution reaction (HER) and oxygen evolution reaction (OER). Effective electrocatalysts must be used to reduce the dynamic overpotentials [3–5]. At present, the most advanced electrocatalysts for HER and OER are platinum-based materials and ruthenium/iridium oxides, respectively [6–7]. However, the application of noble metal-based electrocatalysts is limited because of the high cost and scarce resources. Considerable progress has been made in the development of non-noble metal electrocatalysts [8–11], such as transition metal chalcogenides [12–14], phosphides [15–16], and oxides [2,17–21]. However, most transition metal-based catalysts usually have good catalytic activity for only one reaction (OER or HER). Thus, the electrocatalysts for OER and HER must be prepared through a different route, which leads to an increase in complexity and cost. The design and construction of bifunctional electrocatalysts for both HER and OER are important challenges and have become a research hotspot.

Transition metal sulfides with dual-phase structure and good conductivity, such as Co-doped MoS_2 [21], Fe–Ni_3S_2 [22], Ni_3S_2/Co_3S_4 [23], and NiS/FeS [24], are considered potential bifunctional catalysts. However, metal sulfides only exhibit good activity for HER. The active sites for OER are mainly *in situ* formed by the structure evolution of sulfides to oxides or hydroxides. However, their bifunctional activity and stability are difficult to control. By contrast, transition metal oxides or hydroxides usually exhibit good activity for OER because of the strong adsorption capability of oxygen-containing intermediates [25–27]. However, the catalytic activity for HER is poor. Moreover, the weak conductivity of metal oxides or hydroxides is a limiting issue.

Based on the preceding discussion, the construction of a sulfide/oxide heterostructure may be a promising strategy to achieve good bifunctional activity for HER and OER. Particularly, the transfer and redistribution of electrons can easily occur between iron and nickel, which are similar three-dimensional (3D) transition metals. Thus, the adsorption/desorption of intermediates needs to be optimized [28], which can also improve the catalytic activity. Therefore, Ni–Fe bimetallic sulfide/oxide heterostructures are considered excellent bifunctional catalysts for overall water splitting.

By contrast, water splitting is driven by renewable energy

✉ Corresponding authors: Yiwei Zhong E-mail: ywzhong@ustb.edu.cn; Mingyong Wang E-mail: mywang@ustb.edu.cn

with a fluctuating current. However, powdery catalysts are usually synthesized to increase the effective active sites [29–31] but easily fluctuate at a large current density. Meanwhile, nonconductive binders will cover active sites, which is unfavorable to the rapid transfer of electrons/ions. Recently, self-supporting catalysts without binders, which are usually grown on a smooth substrate, have been proposed [32]. Porous structures are constructed using only catalysts, which results in a poorly effective active area and weak adhesion on the substrate. Thus, growing self-supporting catalysts on a 3D porous substrate may be an effective strategy. Therefore, the adhesion of self-supporting catalysts is expected to improve because of the binding action of the 3D porous substrate. Meanwhile, a hierarchically porous structure can be constructed using both self-supporting porous catalysts and 3D porous substrates.

Here, a novel self-supporting Ni_xFe–S/$NiFe_2O_4$ heterostructure with hierarchically porous nanosheets on 3D porous carbon fiber cloth (CFC) is designed and constructed based on porous Ni–Fe electrodeposition on a gas–liquid–solid interface, *in situ* oxidation, and partial chemical sulfuration. The results confirmed that the Ni_xFe–S/$NiFe_2O_4$ heterostructure exhibited remarkable bifunctional activity for both HER and OER. The cell voltage of overall water splitting using the Ni_xFe–S/$NiFe_2O_4$ heterostructure as both cathode and anode are lower than those of commercial 20wt% Pt/C||IrO_2–Ta_2O_5.

2. Experimental

2.1. Materials

$NiSO_4·6H_2O$ and $FeSO_4·7H_2O$ were purchased from Tianjin Heowns (China) and Shanghai Energy Chemical (China), respectively. $NiCl_2·6H_2O$ and $FeCl_2·4H_2O$ were purchased from Macklin (China). NH_4F, CH_4N_2O, $(NH_4)_2SO_4$, $C_6H_5Na_3O_7·2H_2O$, and $Na_2S·9H_2O$ were purchased from Aladdin (China). All chemical reagents were of analytical grade.

2.2. Synthesis of porous Ni–Fe

The electrolyte was composed of 0.01–0.2 mol·L^{-1} $NiSO_4$, 0.01–0.2 mol·L^{-1} $FeSO_4$, 1 mol·L^{-1} $(NH_4)_2SO_4$, and 0.3 mol·L^{-1} $C_6H_5Na_3O_7$. Carbon fiber cloth (CFC) with an exposed area of 1 cm^2 was used as substrate. Ni–Fe electrodeposition was conducted using a direct current power supply at 3.5 A·cm^{-2} for 45 s. Porous Ni–Fe/CFC was cleaned and dried in a vacuum drying oven.

2.3. Synthesis of $NiFe_2O_4$

Porous Ni–Fe alloy was placed in a muffle furnace, heated to 400°C at 4°C/min in an argon atmosphere for 2 h, and exposed to air at 400°C for 2 h to obtain $NiFe_2O_4$.

2.4. Synthesis of Ni_xFe–S/$NiFe_2O_4$

$NiFe_2O_4$ was immersed in 0.1 mol·L^{-1} $Na_2S·9H_2O$ solution in an 80 mL Teflon-lined stainless steel autoclave. Then, the autoclave was sealed and maintained at 160°C for 6 h. After complete cooling, Ni_xFe–S/$NiFe_2O_4$ was obtained and washed repeatedly with distilled water.

2.5. Synthesis of Ni_xFe–S

Ni–Fe alloy was immersed in a solution containing 0.4–2 mmol·L^{-1} $NiCl_2·6H_2O$, 0.4–2 mmol·L^{-1} $FeCl_2·4H_2O$, 0.1 mol·L^{-1} NH_4F, and 0.2 mol·L^{-1} CH_4N_2O in an 80 mL Teflon-lined stainless steel autoclave. The autoclave was sealed and maintained at 120°C for 6 h. Then, the obtained sample was immersed in a 0.1 mol·L^{-1} $Na_2S·9H_2O$ solution in an 80 mL Teflon-lined stainless steel autoclave. The autoclave was sealed and maintained at 160°C for 6 h. After complete cooling, Ni_xFe–S was obtained and washed repeatedly with distilled water.

2.6. Structure characterizations

The crystalline structures, phases, morphologies, and microstructures were characterized by X-ray diffraction (XRD; Rigaku, D/Max-RB; Cu K_α radiation (λ = 0. 15418 nm)), X-ray photoelectron spectroscopy (XPS; Kratos, Axis Ultra DLD; Al K_α X-ray source), scanning electron microscopy (SEM, JEOL, JSM6510A), and high-resolution transmission electron microscopy (HRTEM; JEOL, JSM-2100F).

2.7. Electrochemical measurements

Electrochemical measurements were conducted at room temperature using the three-electrode system in a CHI 660E electrochemical workstation (CHI Instruments, Shanghai Chenhua Instrument Co., Ltd., Shanghai, China). Saturated Hg/Hg_2Cl_2 in a saturated 1 mol·L^{-1} KOH solution was employed as the reference electrode. The catalysts were used as the working electrode, and a Pt rod was utilized as the counter electrode. The potentials were referenced to the RHE.

2.8. DFT calculation

Metal compounds are usually simplified to metals as active sites during density functional theory (DFT) calculation because of the limitations on the calculation capability [10,33–34]. For example, $Ni(OH)_2$ and $Ce(OH)_2$ are simplified to Ni and Ce [35], respectively. Therefore, $Ni_{1/5}Fe$–S is replaced by Ni-doped Fe_9S_{10}. The heterostructure of $NiFe_2O_4$ and Ni-doped Fe_9S_{10} is constructed to calculate the free energy of hydrogen desorption and compared with those of $NiFe_2O_4$, Ni-doped Fe_9S_{10}, and Fe_9S_{10}.

The DFT framework embedded in the cambridge sequential total energy package (CASTEP) code was employed to investigate the HER of the prepared catalysts. The exchange and correlation energy were processed using the Perdew–Burke–Ernzerhof functional with the generalized gradient approximation form. Spin polarization was included in all calculations. The electronic wave functions at each *k*-point were expanded in terms of a plane-wave basis set, and an energy cutoff of 500 eV was employed. The catalysts were simulated by periodically repeating the $NiFe_2O_4$ layers along the

(400) direction of the unit cell. The same slab of Fe_9S_{10}, in which a surface Fe atom was replaced by a Ni atom to simulate nickel sulfide species, was employed. Structures were optimized by the Broyden–Fletcher–Goldfarb–Shanno method, and the geometric mean procedure was repeated until the average force on the atoms was <0.3 eV/nm and the energy change was $<5.0 \times 10^{-6}$ eV/atom.

3. Results and discussion

3.1. Preparation and characterization of the Ni_xFe–S/$NiFe_2O_4$ heterostructure

A self-supporting and hierarchically porous Ni_xFe–S/$NiFe_2O_4$ heterostructure with nanosheets was constructed and illustrated in Fig. 1(a). First, porous Ni–Fe alloys with microparticles were electrodeposited on 3D porous carbon fiber cloth by the bubble template method to obtain a large specific surface area (Fig. S1(a) and (b)). Then, porous Ni–Fe alloy is *in situ* oxidized in air to $NiFe_2O_4$ with needle-like nanosheets, which are partially perpendicular to the substrate (Fig. S1(c) and (d)). Finally, the surface oxide layer is partially converted into sulfide by the *in situ* chemical sulfuration reaction in Na_2S solution. According to the ΔG (Gibbs free energy) values of Reactions S1 to S4 in the Supporting Information, the sulfuration reactions proceed spontaneously.

Therefore, the Ni_xFe–S/$NiFe_2O_4$ heterostructure consisting of nanosheets is obtained (Fig. 1(b) and (c)). Figs. 1(b) and S1(e) show that thin Ni_xFe–S nanosheets evenly and firmly wrap the surface of carbon fibers. Therefore, the hierarchically porous structure is constructed by 3D porous carbon fiber cloth and porous nanosheets. This structure will provide a large electrochemically active surface area in 3D space, which increases the active sites and promotes the effective transfer of electrons/ions. A micro/nanostructure can accelerate the separation of bubbles to ensure the continuous exposure of active sites and the stability of the structure un-

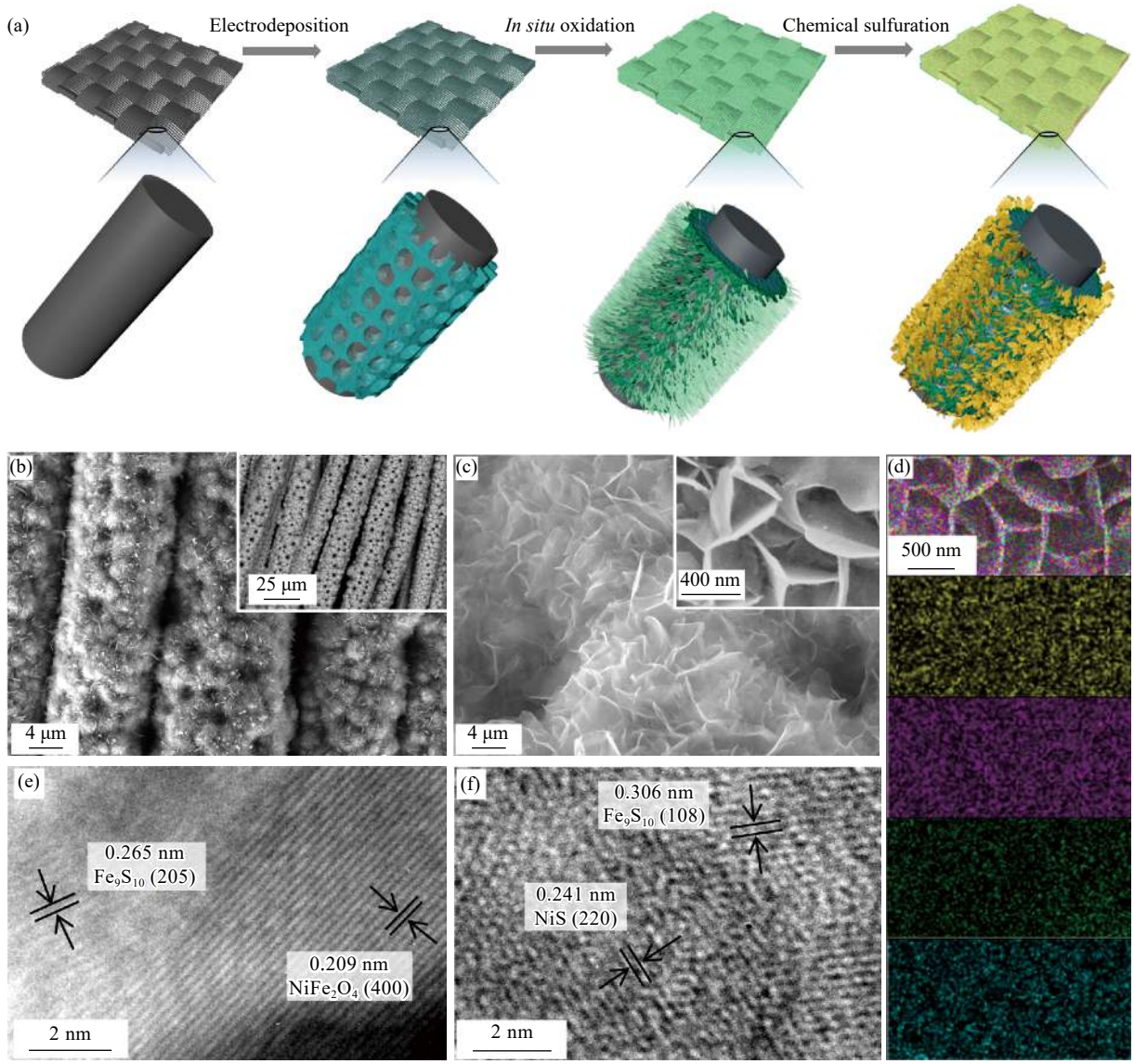

Fig. 1. (a) Illustration of the preparation of a self-supporting and hierarchically porous Ni_xFe–S/$NiFe_2O_4$ heterostructure. (b, c) SEM images of $Ni_{1/2}Fe$–S/$NiFe_2O_4$. (d) Energy-dispersive spectroscopy elemental mapping images of $Ni_{1/2}Fe$–S/$NiFe_2O_4$. (e, f) HRTEM images of $Ni_{1/2}Fe$–S/$NiFe_2O_4$.

der a high current density.

According to a previous study [35], the nickel/iron (Ni/Fe) ratio has a considerable influence on the morphology and electrocatalytic performance. Therefore, the Ni/Fe ratio in $Ni_xFe–S/NiFe_2O_4$ is adjusted by changing the Ni^{2+}/Fe^{2+} ratio in the electrodeposition solution. x in $Ni_xFe–S/NiFe_2O_4$ represents the molar ratio of nickel sulfate to [nickel sulfate + ferrous sulfate] in the electrodeposition solution. For single-metal Fe–S/Fe_2O_3 heterostructures (Fig. S2(a)), the nanosheets are thin and cannot be completely grown on the surface of catalysts. For bimetallic $Ni_xFe–S/NiFe_2O_4$ heterostructures, the nanosheets become uniform on the surface of catalysts (Fig. S2(b)–(d)). However, for Ni–S/Ni–O (Fig. S2(e)), the nanosheets with large thickness are disorderly. Fig. 1(d) shows the energy-dispersive spectroscopy (EDS) elemental mapping image of $Ni_{1/2}Fe–S/NiFe_2O_4$. Ni, Fe, S, and O are uniformly distributed. The HRTEM images (Fig. 1(e) and (f)) confirmed that oxides and sulfides coexist. Particularly, both NiS and Fe_9S_{10} [36–38] are detected on the obtained nanosheets (Fig. 1(f)), which helps improve the intrinsic activity of sulfides because of the synergistic effect.

The XRD patterns shown in Fig. 2(a) further confirm the successful synthesis of the $Ni_xFe–S/NiFe_2O_4$ heterostructure. Notably, $FeNi_3$ alloys corresponding to the diffraction peaks at 44.2°, 51.5°, and 75.8° are electrodeposited. After oxidation, the peaks at 35.7°, 53.8°, 57.4°, and 63.0° appear because of the formation of the $NiFe_2O_4$ oxide layer. Meanwhile, the peaks at 33.1°, 40.8°, 49.4°, and 63.9° indicate that Fe_2O_3 is also formed. After chemical sulfuration, all peaks corresponding to Fe_2O_3 disappear, and the peak intensity of $NiFe_2O_4$ decreases. This finding indicates that all Fe_2O_3 and partial $NiFe_2O_4$ are converted into sulfides. The peaks at 33.8°, 43.7°, and 57.8° corresponding to Fe_9S_{10} and the peaks at 35.6°, 37.3°, 59.7°, 56.3° and 57.4° corresponding to NiS are observed. These results are consistent with those of the HRTEM images shown in Fig. 1(f). That is, the $Ni_xFe–S/NiFe_2O_4$ heterostructure with nanosheets is successively constructed.

To further investigate the surface chemical composition and valence states of $Ni_xFe–S/NiFe_2O_4$, XPS depth profiling

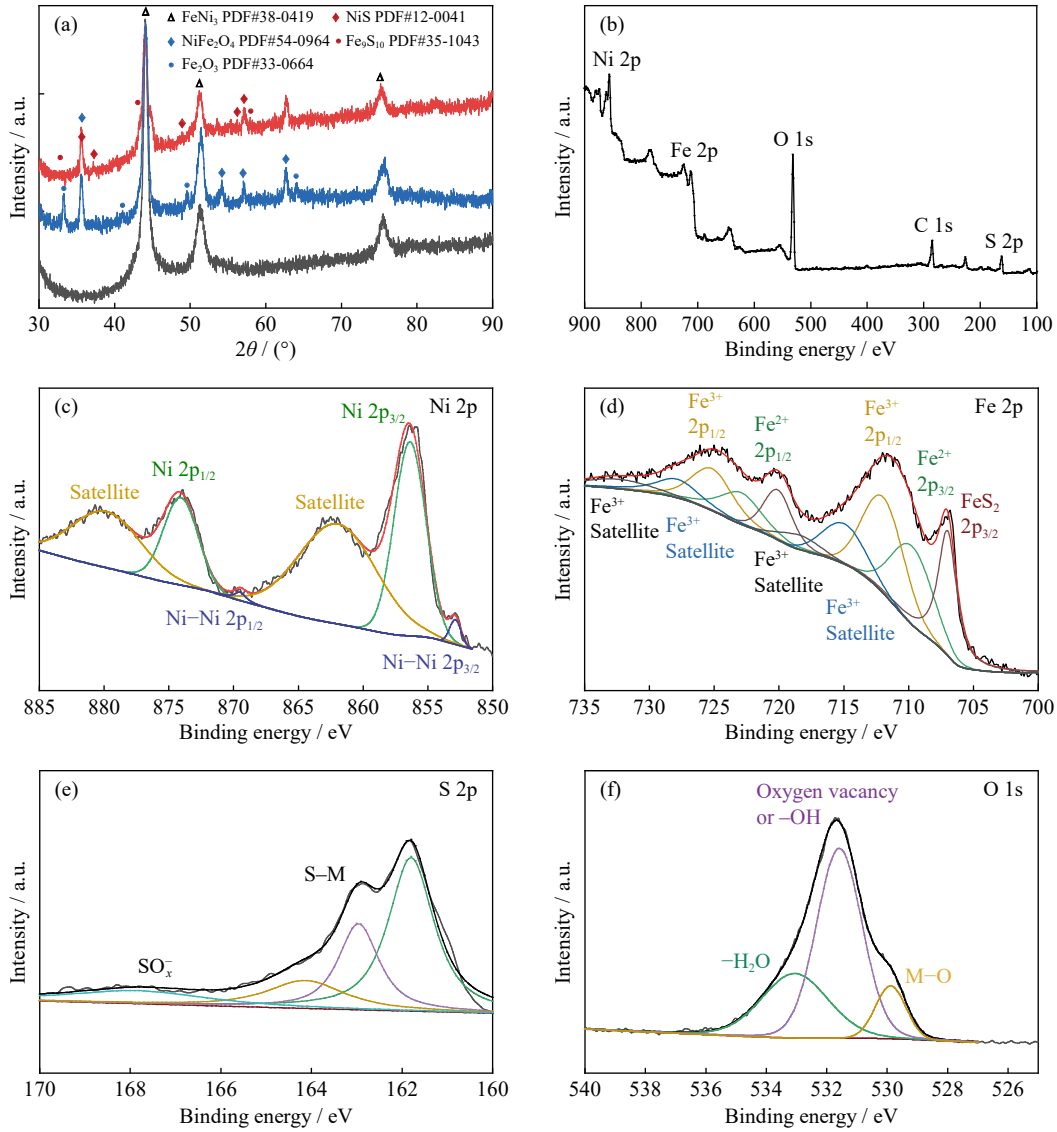

Fig. 2. (a) XRD patterns of products obtained at different preparation stages, (b) XPS overall spectra of $Ni_{1/2}Fe–S/NiFe_2O_4$, and high-resolution XPS spectra of (c) Ni, (d) Fe, (e) S, and (f) O in $Ni_{1/2}Fe–S/NiFe_2O_4$.

analysis was conducted (Fig. 2(b)). The signals of Ni, Fe, S, and O appear in the XPS overall spectra of Ni_xFe–S/$NiFe_2O_4$ and match well with those of the XRD and EDS elemental mapping images. Specifically, in the Ni 2p spectrum (Fig. 2(c)), the peaks at 856.4 eV are ascribed to Ni $2p_{3/2}$ of bivalent Ni in $NiFe_2O_4$ and NiS [39–40]. The peaks at 852.8 eV are ascribed to the continuous network of Ni–Ni bonds in the NiS crystal structure, which is related to the metallicity of NiS [41].

The XPS spectrum of Fe 2p is shown in Fig. 2(d). The peaks of Fe $2p_{3/2}$ located at 709.7 eV correspond to Fe^{2+} [42]. The peaks located at 711.9 eV correspond to Fe^{3+} [8]. Moreover, a peak at 707.0 eV corresponding to Fe in FeS_2 can be detected [43–44]. This finding indicates that complex iron–sulfur compounds are obtained. As a result, Fe_9S_{10}, which is composed of FeS and FeS_2, is formed. In the XPS spectrum of S 2p shown in Fig. 2(e), the fitted peaks at 161.8, 163.0, 164.2, and 168.0 eV originated from S $2p_{3/2}$, S $2p_{1/2}$ of sulfide, polysulfide (M is Fe and Ni), and thiosulfate species, respectively. These types of bonds are typical characteristics of metal sulfides [45]. The O 1s spectrum (Fig. 2(f)) has three main peaks: metal–O at 529.9 eV, unsaturated oxygen or oxygen in the hydroxyl group (–OH) at 531.6 eV, and adsorbed H_2O at 533.1 eV [46]. The formation of oxygen vacancy and possible –OH is related to the surface hydrolysis and sulfur intercalation of $NiFe_2O_4$ during hydrothermal chemical sulfuration. The existence of oxygen vacancy is also beneficial to interfacial electron transfer [47]. The XPS results confirm that Ni–Fe oxides and sulfides exist, which proves the formation of the Ni_xFe–S/$NiFe_2O_4$ heterostructure. These results are consistent with those of XRD and HRTEM analyses.

3.2. OER performance of Ni_xFe–S/$NiFe_2O_4$

The electrocatalytic activity of the Ni_xFe–S/$NiFe_2O_4$ heterostructure for OER was evaluated using linear scanning voltammogram (LSV) and electrochemical impedance spectroscopy (EIS) in 1 mol·L^{-1} KOH. To decrease the influence of surface oxidation [48] or the capacitance caused by the transition metal sulfide and hydroxyl groups [49], a low scanning rate of 2 mV·s^{-1} is used. The LSV curves were obtained under the same conditions by both forward and reverse scans to ensure the accuracy of the results [50].

Figs. 3(a), S3, and S4 and Table S1 show that the $Ni_{1/2}Fe$–S/$NiFe_2O_4$ heterostructure exhibits the best electrocatalytic activity. The overpotential (E) is 248 mV at a current density (i) of 10 mA·cm^{-2}, and this value is lower than those of the precursor $NiFe_2O_4$ (η_{10} = 321 mV) and porous Ni–Fe (η_{10} = 358 mV). These results indicate that the synthesis strategy can feasibly improve the catalytic activity. Moreover, $Ni_{1/2}Fe$–S/$NiFe_2O_4$ shows better catalytic activity than $Ni_{1/2}Fe$–S. This finding indicates that the heterostructure of oxide/sulfide helps enhance the catalytic activity for OER. Meanwhile, compared with single-metal heterostructures of Ni–S/NiO and Fe–S/Fe_2O_3, bimetallic heterostructures of $Ni_{1/2}Fe$–S/$NiFe_2O_4$ exhibit better activity for OER, which can be ascribed to the synergistic effects of nickel and iron.

The Tafel curves were also obtained to evaluate the reaction kinetics. As shown in Fig. 3(b), $Ni_{1/2}Fe$–S/$NiFe_2O_4$ has the lowest Tafel slope of 53 mV·dec^{-1}, which is less than those of $Ni_{1/2}Fe$–S (79 mV·dec^{-1}), $NiFe_2O_4$ (75 mV·dec^{-1}), Ni–S/NiO (94 mV·dec^{-1}), and Fe–S/Fe_2O_3 (102 mV·dec^{-1}) and even lower than that of commercial IrO_2–Ta_2O_5. These results further confirm that the bimetallic $Ni_{1/2}Fe$–S/$NiFe_2O_4$ heterostructure can improve the reaction kinetic of OER, which can be related to good conductivity, hierarchically porous structure, and oxide/sulfide heterostructure. Moreover, bimetal Ni–Fe plays a key role in the adsorption–desorption balance of oxygen-containing intermediates [51]. The electron transfer resistances of OER were analyzed by EIS. As shown in Fig. 3(c), the $Ni_{1/2}Fe$–S/$NiFe_2O_4$ heterostructure shows the smallest electron transfer resistance, which leads to better catalytic activity.

Furthermore, the electrochemically active surface areas of various catalysts were evaluated via the double-layer capacitance (C_{dl}) (Fig. S5), and the results are shown in Fig. 3(d) and Table S1. Notably, Ni_xFe–S/$NiFe_2O_4$ heterostructures have larger C_{dl} values than homogenous structures and single-metal heterostructures. Particularly, the C_{dl} value of $Ni_{1/2}Fe$–S/$NiFe_2O_4$ is the largest (i.e., up to 40.8 mF·cm^{-2}), which can be ascribed to the hierarchically porous structure and uniform nanosheets (Fig. 1(a) and (c), and Figs. S1 and S2). A large C_{dl} value means a highly effective active area. Therefore, the $Ni_{1/2}Fe$–S/$NiFe_2O_4$ heterostructure exhibits good electrocatalytic activity for OER.

Stability is another important parameter used to evaluate catalytic performance. Fig. S6 shows that the $Ni_{1/2}Fe$–S/$NiFe_2O_4$ heterostructure exhibits good stability over 33 h. Water electrolysis is driven by renewable energy with a fluctuating current. Therefore, the chronopotentiometry curve with multi-current step is obtained to investigate the long-term stability of $Ni_{1/2}Fe$–S/$NiFe_2O_4$ for OER (Fig. 3(e)). The current density is initially increased from 10 to 500 mA·cm^{-2} and subsequently decreased to 10 mA·cm^{-2}. As shown in Fig. 3(e), for each current increment, the potential becomes stable immediately and no obvious fluctuating is observed. Moreover, a similar potential is observed at the same current density during the reverse process. The LSV curve (inset in Fig. 3(e)) shows that the catalytic activity of $Ni_{1/2}Fe$–S/$NiFe_2O_4$ for OER is retained after approximately 33 h. These results indicate that $Ni_{1/2}Fe$–S/$NiFe_2O_4$ exhibits excellent activity and stability because of the self-supporting and hierarchically porous heterostructure.

Aside from the intrinsic properties and microstructure, the activity and stability of catalysts are related to wettability. The contact angles of $Ni_{1/2}Fe$–S/$NiFe_2O_4$ and CFC were measured and compared (Fig. 3(f)). Notably, a superhydrophilic surface is observed on the $Ni_{1/2}Fe$–S/$NiFe_2O_4$ heterostructure because of the hierarchically micro/nanoporous structure. Moreover, good wettability can accelerate bubble separation from the catalyst surface and decrease the ohmic resistance [52–53]. Therefore, the overpotential of OER is re-

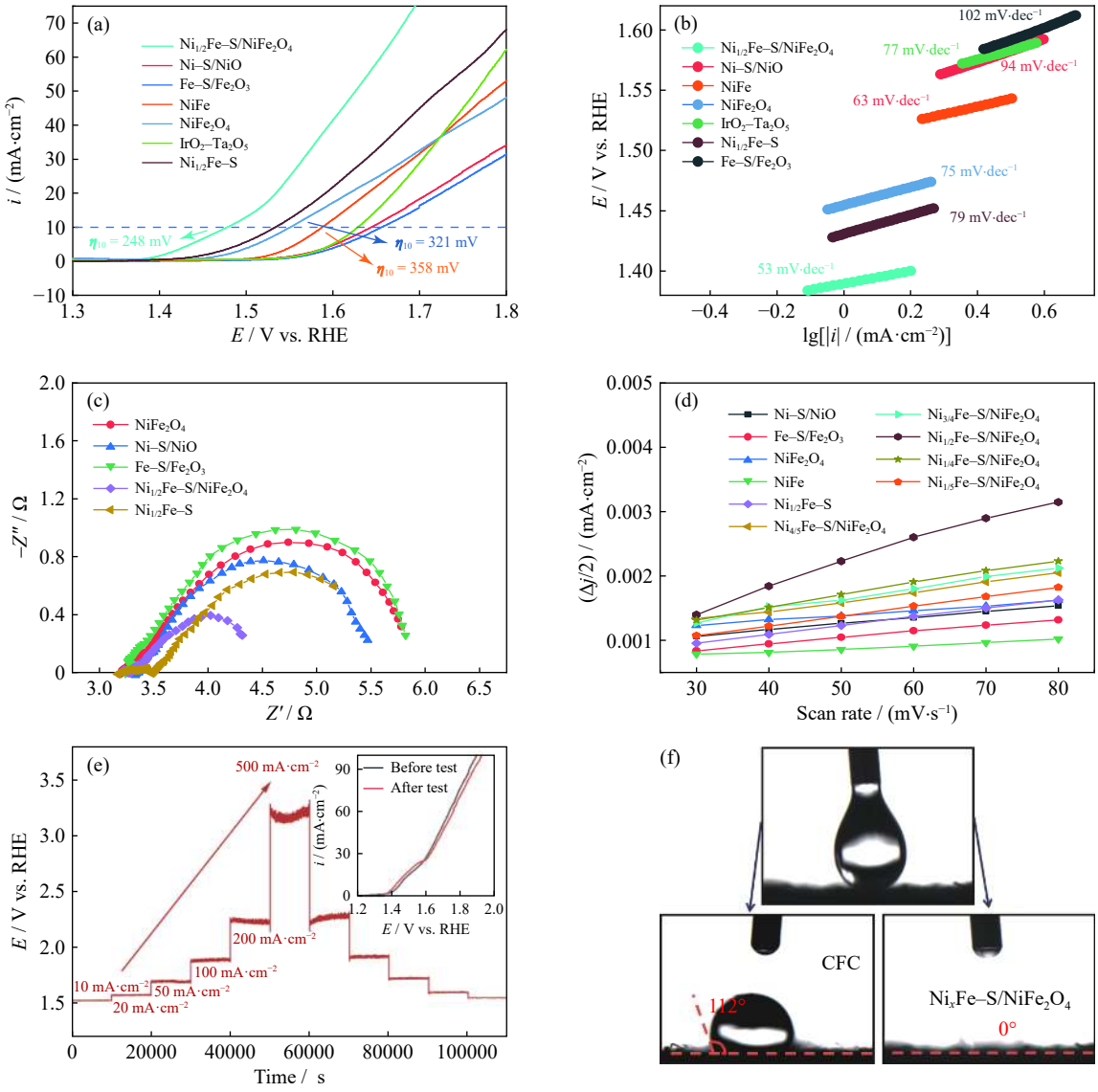

Fig. 3. OER performance: (a) linear scanning voltammogram (LSV) and (b) Tafel plots obtained by forward scan, (c) Nyquist plots, (d) plots of scanning current difference (Δ*j*) at −0.55 V as a function of the scanning rate, (e) chronopotentiometry curve of the $Ni_{1/2}Fe–S/NiFe_2O_4$ heterostructure at various current densities, (f) contact angles of $Ni_{1/2}Fe–S/NiFe_2O_4$ and carbon fiber cloth.

duced and the stability is improved.

Furthermore, during OER, $Ni_{1/2}Fe–S$ in the $Ni_{1/2}Fe–S/NiFe_2O_4$ heterostructure will be inevitably reconstructed *in situ* because of a high oxidation environment. Fig. 4(a) shows that the profile of nanosheets remains the same after the 18-h OER test. However, many nanoclusters are generated at the edge of the original nanosheets. To understand the improvement mechanism of OER performance, the real active sites need to be explored. The surface morphology and electron structure of $Ni_{1/2}Fe–S/NiFe_2O_4$ are further examined by cyclic voltammetry (CV), XRD, and XPS. Fig. S7 shows that six oxidation peaks are detected in the first cycle and the oxidation peaks at approximately 0, 0.65, and 1.3 V disappear after three cycles. These results confirm that rapid *in situ* conversion on the surface of $Ni_{1/2}Fe–S/NiFe_2O_4$ occurs in the early CV activation process. The surface composition of stable catalysts is different from the original $Ni_{1/2}Fe–S/NiFe_2O_4$.

XRD tests were conducted to further understand the structure evolution. Fig. 4(b) shows that the characteristic peaks of NiS become weak and the characteristic peaks of Ni_3S_2 appear after 10 min. Meanwhile, the characteristic peaks of Fe_9S_{10} disappear completely. With the increase of the test time to 18 h, the characteristic peak of Ni_3S_2 becomes sharper, which indicates that the crystallinity or content of Ni_3S_2 is enhanced. The new characteristic peak at 21.2° corresponding to FeOOH appears. That is, Fe_9S_{10} is converted into FeOOH. Specifically, in the $Ni_{1/2}Fe–S/NiFe_2O_4$ heterostructure, Fe_9S_{10} is more easily oxidized to oxides/hydroxides than NiS. After a short test time, FeS is completely oxidized and transformed into amorphous and fine FeOOH nanosheets. A similar phenomenon is reported in a previous study [54]. However, NiS is not completely oxidized and converted into Ni_3S_2 because of S migration and surface oxidation. Moreover, the peaks of $NiFe_2O_4$ are reduced. According to several reports in the literature [55–56], $NiFe_2O_4$ exposed on the surface will be hydrolyzed and converted into hydroxide or further converted into hydroxyl oxide during OER. The hydroxides or hydroxyl oxides converted from sulfides or ox-

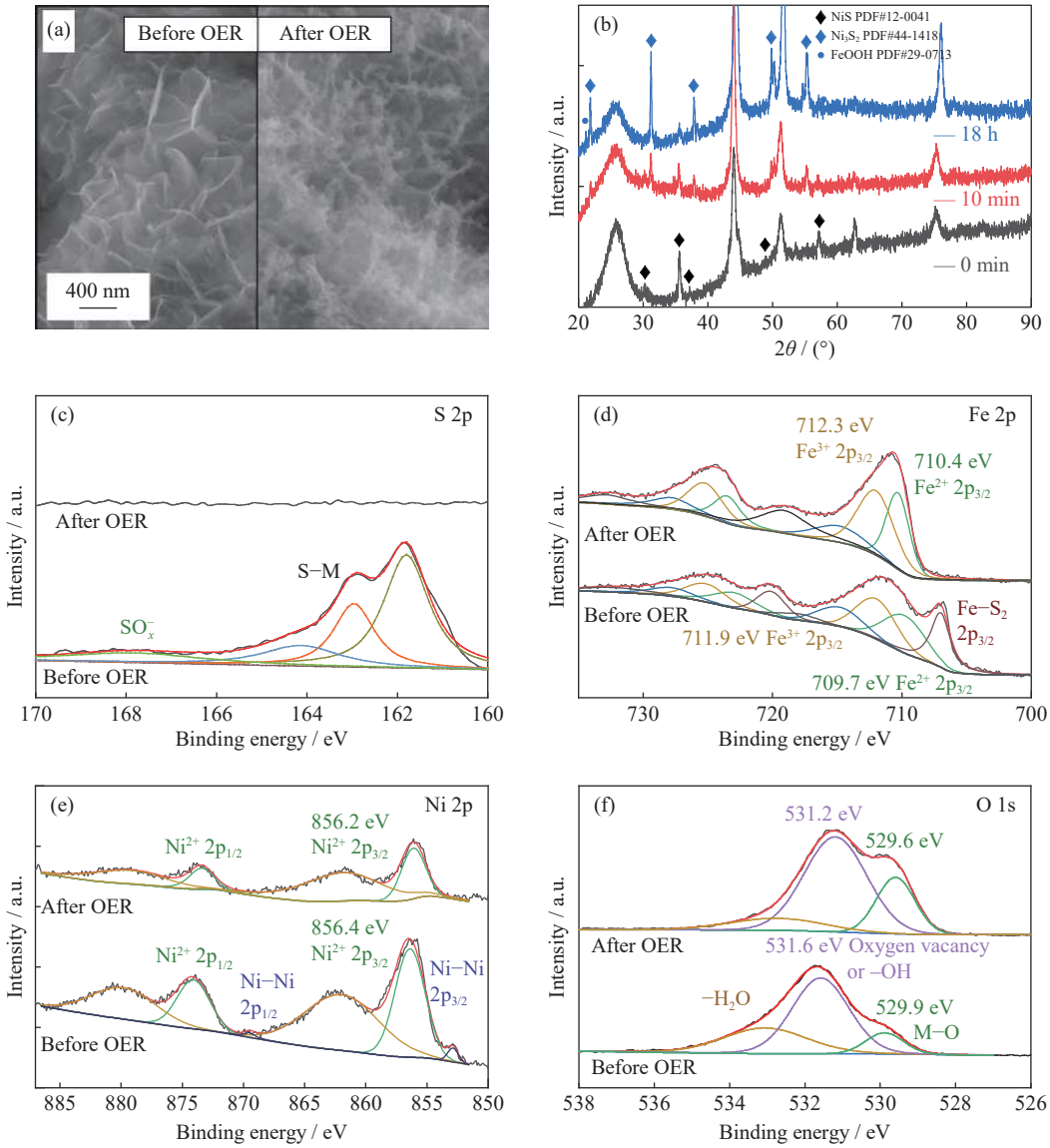

Fig. 4. (a) SEM images of the $Ni_{1/2}Fe–S/NiFe_2O_4$ heterostructure before and after the 18 h OER test, (b) XRD patterns after 0 min, 10 min, and 18 h, and (c–f) XPS spectra of S, Fe, Ni, and O.

ides may serve as active species for OER. Meanwhile, the residual sulfides can increase the conductivity to improve the catalytic activity.

XPS was conducted to further understand the transformation of the surface composition and chemical valence of $Ni_{1/2}Fe–S/NiFe_2O_4$ during OER. As shown in Fig. 4(c), after the 18-h OER test, only weak S 2p peaks can be identified. This finding indicates that most of the S on the surface is oxidized and removed. As shown in Fig. 4(d), the Fe $2p_{3/2}$ peak at 707.0 eV corresponding to Fe–S_2^{2-} disappears after the 18-h OER test [40,43]. Meanwhile, the Fe^{3+} $2p_{3/2}$ peak shifts to higher binding energies. The peak change is consistent with the transformation from Fe–S bond to Fe–O bond, which may correspond to the conversion of Fe^{2+} into Fe^{3+} in FeOOH because of the high oxidation conditions. Fig. 4(d) shows that the peak intensity of the Ni 2p spectrum decreases after the 18-h OER test, which indicates that the distribution of nickel on the surface is changed. Specifically, the Ni–Ni bond disappears, and the intensity of the Ni^{2+} peak shifts to the right. This result is inconsistent with that obtained by XRD. If all NiS components are converted into Ni_3S_2, then the strength of the Ni–Ni bond should be stronger than that before the 18-h OER test. This finding indicates that Ni may not exist in the form of Ni_3S_2. Moreover, the nickel-based oxide or hydroxide species cannot be easily detected by XRD. Nickel oxides mainly exist on the catalyst surface because of phase transformation during OER. Ni species is doped into iron oxide species. Because of the larger detection depth of XRD than XPS, we inferred that Ni_3S_2 mainly exists on the inside, whereas nickel oxide and FeOOH are located on the surface during oxidation conversion. The XPS spectrum of O 1s is shown in Fig. 4(f). The peak intensity corresponding to M–O increases significantly after the 18-h OER test, which illustrates the formation of metal oxide species. Furthermore, the peak intensity corresponding to –OH increases and shifts to the left, which indicates that Ni–Fe sulfides and $NiFe_2O_4$ are partially converted into hydroxyl oxides.

According to the previously presented results, we can con-

clude that the $Ni_{1/2}Fe$–S phase in $Ni_{1/2}Fe$–S/$NiFe_2O_4$ heterostructure is significantly reconstructed during OER. Fe_9S_{10} and NiS undergo irreversible oxidation reactions and are finally transformed into metal oxides/hydroxides (such as FeOOH) and Ni_3S_2. Ni_3S_2 is mainly located inside the catalysts, whereas the fine metal oxide/hydroxide nanoclusters grow on the surface. Fe hydroxide species are dominant on the surface. Fine nanoparticles generated on the surface of nanosheets can increase the surface area and provide a large reaction interface. By contrast, high valence oxides have higher activity and stability. Ni_3S_2 at the bottom of FeOOH has high conductivity, which is beneficial to electron transfer. After a long-term OER test, the crystallinity of catalysts is enhanced (Fig. 4(b)), which also indicates the improvement of stability. Therefore, the special self-supporting hierarchically porous heterostructure obtained by *in situ* transformation during the OER process exhibits good catalytic activity.

3.3. HER performance of Ni_xFe–S/$NiFe_2O_4$

The electrocatalytic activity of the self-supporting Ni_xFe–S/$NiFe_2O_4$ heterostructure for HER is evaluated in 1 mol·L^{-1} KOH solution. Among all Ni_xFe–S/$NiFe_2O_4$ heterostructures, $Ni_{1/5}Fe$–S/$NiFe_2O_4$ exhibits the best HER activity (Fig. S8). Meanwhile, Fig. 5(a) shows that compared with single-metal heterostructures (i.e., Ni–S/NiO and Fe–S/Fe_2O_3) and bimetallic single-phase structures (i.e., $Ni_{1/5}Fe$–S and $NiFe_2O_4$), bimetallic $Ni_{1/5}Fe$–S/$NiFe_2O_4$ heterostructures exhibit better activity because of the synergistic effect. Moreover, Fe–S/Fe_2O_3 is unstable and easily oxidized in air. Therefore, a reduction peak from Fe^{3+} appears in Fig. 5(a). The Tafel results further confirm the conclusion (Fig. 5(b)). The Tafel slope of $Ni_{1/5}Fe$–S/$NiFe_2O_4$ is low, which indicates that the interface of the bimetallic heterostructure can improve the reaction kinetics. Furthermore, according to the Nyquist plots (Fig. S9), $Ni_{1/5}Fe$–S/$NiFe_2O_4$ exhibits the smallest charge transfer resistance.

Notably, the activity difference between $Ni_{1/5}Fe$–S/$NiFe_2O_4$ heterostructure and 20wt% Pt/C decreased gradually with the increase of current density (Fig. 5(a)). Particularly, at a higher current density than 100 mA·cm^{-2}, the activity of $Ni_{1/5}Fe$–S/$NiFe_2O_4$ is higher than that of 20wt% Pt/C. The reaction overpotentials of HER are related to catalytic activity and ohmic resistance. The adsorption of nonconductive bubbles on the electrode surface will lead to a large ohmic resistance. As shown in Fig. 3(f), the micro/nanoporous structure of $Ni_{1/5}Fe$–S/$NiFe_2O_4$ provides more active sites and brings about better wettability. The separation radius of bubbles is decreased [50,57]. Specifically, at a large current density, the coverage rate and ohmic resistance of bubbles on the surface decrease, and the active sites are more easily exposed. Therefore, the catalytic activity of the $Ni_{1/5}Fe$–S/$NiFe_2O_4$ heterostructure is markedly improved.

Moreover, to clarify the activity improvement mechanism of the bimetallic heterostructure, the DFT calculation was conducted. HER is usually divided into two main steps: water dissociation (Volmer step) and hydrogen desorption (Heyrovsky or Tafel step) [53,58]. According to the Tafel slopes shown in Fig. 5(b), H^* desorption is the limiting step

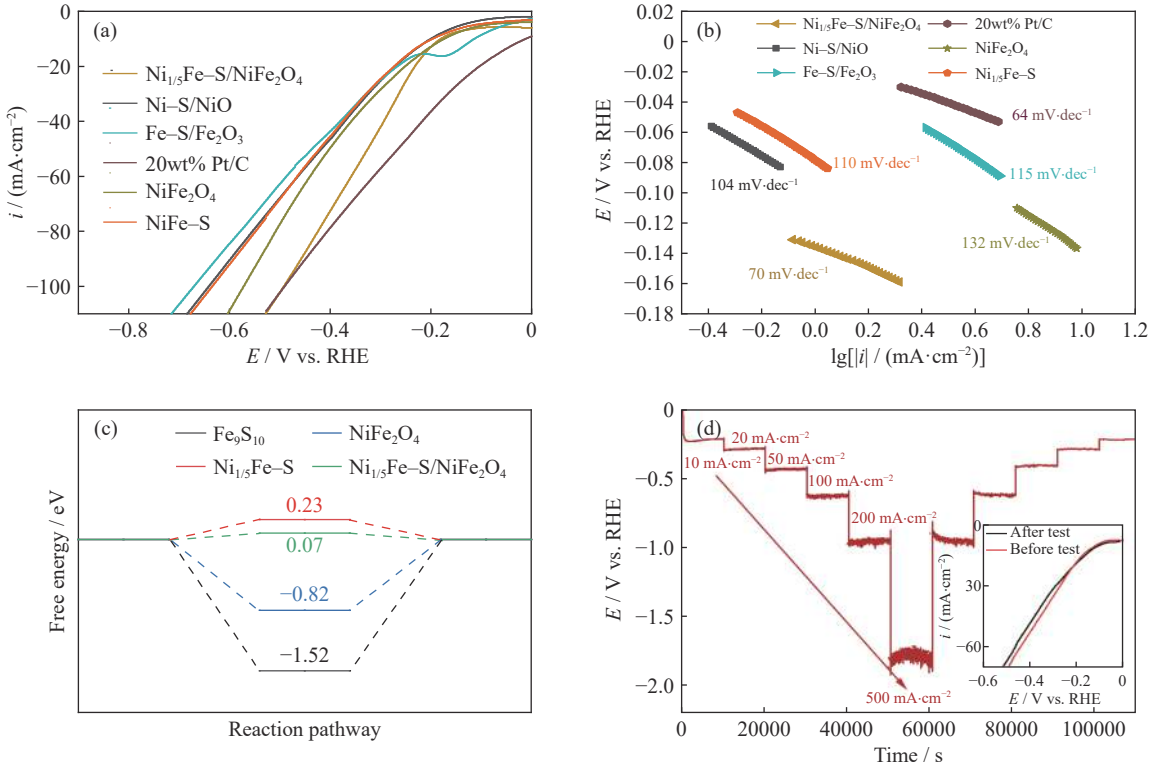

Fig. 5. HER performance in 1 mol·L^{-1} KOH solution: (a) LSV curves, (b) Tafel plots, (c) free energy (ΔG_{H^*}) of H* desorption on the surfaces of Fe_9S_{10}, $Ni_{1/5}Fe$–S, $NiFe_2O_4$, and $Ni_{1/5}Fe$–S/$NiFe_2O_4$, and (d) chronopotentiometry curve of the $Ni_{1/5}Fe$–S/$NiFe_2O_4$ heterostructure at various current densities.

[59]. Therefore, the free energy (ΔG_{H^*}) of H^* desorption on various catalysts is calculated. As shown in Fig. 5(c), the ΔG_{H^*} value of H^* species on $Ni_{1/5}Fe$–S/$NiFe_2O_4$ is only 0.07 eV, which is favorable to the formation of H_2. By contrast, the ΔG_{H^*} values of Fe_9S_{10}, $NiFe_2O_4$, and $Ni_{1/5}Fe$–S are either too smaller or too large (ΔG_{H^*} = −1.52, −0.82, and 0.23 eV), which leads to a sluggish hydrogen reaction. Therefore, the bimetallic heterostructure of $Ni_{1/5}Fe$–S/$NiFe_2O_4$ exhibits good catalytic activity for HER.

The stability of the self-supporting $Ni_{1/5}Fe$–S/$NiFe_2O_4$ heterostructure was evaluated. As shown in Fig. S10, the potentials at 20 mA·cm^{-2} gradually decrease and tend to be stable at the initial stage, which may be related to surface activation. Stability is also evaluated at fluctuating current density, and the results are shown in Fig. 5(d). Good stability of the self-supporting $Ni_{1/5}Fe$–S/$NiFe_2O_4$ heterostructure is obtained at successive current steps. After the current step to 500 mA·cm^{-2}, the current densities are recovered. The potentials are still stable and similar at the same current densities. The polarization curves before and after stability measurement (inset in Fig. 5(d)) show that the activity of $Ni_{1/5}Fe$–S/$NiFe_2O_4$ decreased slightly. These results indicate that the $Ni_{1/5}Fe$–S/$NiFe_2O_4$ heterostructure exhibits good activity and stability for HER.

3.4. Overall water splitting performance of bifunctional Ni_xFe–S/$NiFe_2O_4$

The previously presented results confirm that self-supporting hierarchically porous Ni_xFe–S/$NiFe_2O_4$ heterostructures exhibit excellent bifunctional activities for both HER and OER. Therefore, an overall water splitting cell is constructed using $Ni_{1/5}Fe$–S/$NiFe_2O_4$ as cathode for HER and $Ni_{1/2}Fe$–S/$NiFe_2O_4$ as anode for OER (Fig. S11). For comparison, commercial 20wt% Pt/C||IrO_2–Ta_2O_5 is also measured. The LSV curves are shown in Fig. 6(a). Notably, 20wt% Pt/C||IrO_2–Ta_2O_5 still shows better catalytic activity at a lower current density. However, when the current density exceeds approximately 33 mA·cm^{-2}, $Ni_{1/5}Fe$–S/$NiFe_2O_4$||$Ni_{1/2}Fe$–S/$NiFe_2O_4$ shows better catalytic activity than 20wt% Pt/C||IrO_2–Ta_2O_5. These properties can be attributed to the heterostructure and good wettability of the hierarchically porous structure, which promotes bubble separation. Therefore, the ohmic resistance of $Ni_{1/5}Fe$–S/$NiFe_2O_4$||$Ni_{1/2}Fe$–S/$NiFe_2O_4$ is decreased, and the effective active sites are well exposed, even at a high current density.

To simulate the practical application environment, the chronopotentiometry curve is also tested at successive current steps. As shown in Fig. 6(b), at all current densities, the cell voltages of $Ni_{1/5}Fe$–S/$NiFe_2O_4$||$Ni_{1/2}Fe$–S/$NiFe_2O_4$ are more stable and lower than those of 20wt% Pt/C||IrO_2–Ta_2O_5. Particularly, the cell voltage difference increases as a function of current density. At 500 mA·cm^{-2}, the cell voltage of $Ni_{1/5}Fe$–S/$NiFe_2O_4$||$Ni_{1/2}Fe$–S/$NiFe_2O_4$ is only approximately 3.91 V, whereas that of the 20wt% Pt/C||IrO_2–Ta_2O_5 electrolyzer is approximately 4.79 V. Moreover, at a current density larger than 50 mA·cm^{-2}, the voltage curve of 20wt% Pt/C||IrO_2–Ta_2O_5 fluctuates periodically because of the rapid growth and separation of large bubbles on the electrode surface. However, the cell voltages of $Ni_{1/5}Fe$–S/$NiFe_2O_4$||$Ni_{1/2}Fe$–S/$NiFe_2O_4$ are relatively stable, even at a large current density of 500 mA·cm^{-2}. Furthermore, $Ni_{1/5}Fe$–S/$NiFe_2O_4$||$Ni_{1/2}Fe$–S/$NiFe_2O_4$ maintains nearly similar cell voltages at the same current density during the increase and decrease of current density. However, 20wt% Pt/C||IrO_2–Ta_2O_5 cannot maintain the original activity. The powdery catalysts in 20wt% Pt/C||IrO_2–Ta_2O_5 must be loaded on the current collector by binders. The adhesion between the catalyst and the current collector is weaker than that of the self-supporting Ni_xFe–S/$NiFe_2O_4$ heterostructure. During the current step at a large current density, the powdery catalysts will drop from the current collector because of the intense attack of bubbles. However, Ni_xFe–S/$NiFe_2O_4$ is still stable because of the self-supporting structure and good wettability. These results confirm that the self-supporting Ni_xFe–S/$NiFe_2O_4$ heterostructure exhibits excellent catalytic activity and stability, even superior to those of commercial noble metal catalysts.

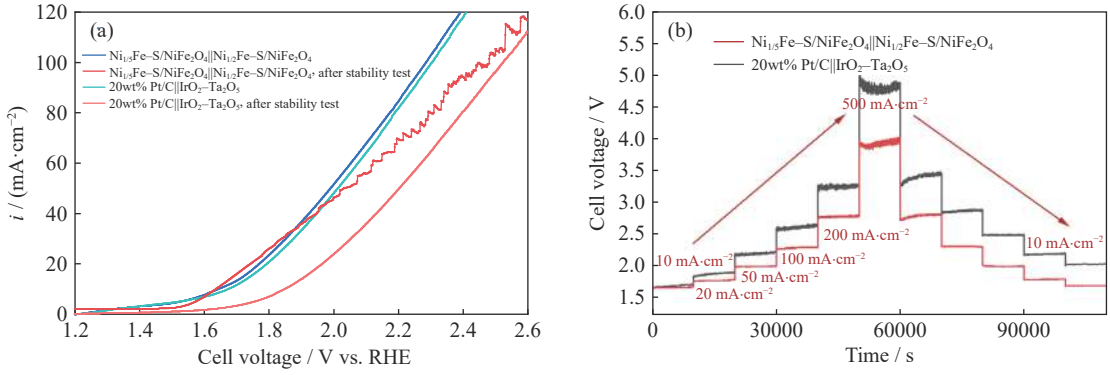

Fig. 6. Overall water splitting in 1 mol·L^{-1} KOH solution: (a) LSV curves of $Ni_{1/5}Fe$–S/$NiFe_2O_4$||$Ni_{1/2}Fe$–S/$NiFe_2O_4$ and 20wt% Pt/C||IrO_2–Ta_2O_5; (b) chronopotentiometry curves of $Ni_{1/5}Fe$–S/$NiFe_2O_4$||$Ni_{1/2}Fe$–S/$NiFe_2O_4$ and 20wt% Pt/C||IrO_2–Ta_2O_5.

4. Conclusions

A novel self-supporting hierarchically porous Ni_xFe–S/$NiFe_2O_4$ heterostructure as a bifunctional electrocatalyst for fluctuating overall water splitting is designed and synthesized on 3D carbon fiber cloth by the Ni–Fe electrodeposition,

oxidation, and chemical sulfuration. Compared with single-metal heterostructures and homogeneous structures, bimetallic Ni_xFe–S/$NiFe_2O_4$ heterostructures exhibit better catalytic activity for both OER and HER because of the abundance of active sites and the synergistic effect of the heterostructure. Notably, the Ni_xFe–S phase in the optimum $Ni_{1/2}Fe$–S/$NiFe_2O_4$ heterostructure is transformed into metal oxides/hydroxides and Ni_3S_2 as active sites for OER. The $Ni_{1/5}Fe$–S/$NiFe_2O_4$ heterostructure exhibits the best catalytic activity for HER. The $Ni_{1/5}Fe$–S/$NiFe_2O_4$||$Ni_{1/2}Fe$–S/$NiFe_2O_4$ electrolyzer exhibits better stability and lower cell voltages at fluctuating current density than the commercial 20wt% Pt/C||IrO_2–Ta_2O_5 electrolyzer because of its self-supporting structure, good activity, and superhydrophilic surface. This work provides a promising strategy to design and construct efficient non-noble metal electrocatalysts for fluctuating overall water splitting.

Acknowledgements

This work was financially supported by the National Natural Science Foundation of China (Nos. 51874020 and 52004022).

Conflict of Interest

The authors declare no conflict of interest.

Supplementary Information

The online version contains supplementary material available at https://doi.org/10.1007/s12613-022-2443-2.

References

[1] X.S. Wang, Y. Zheng, W.C. Sheng, Z.J. Xu, M. Jaroniec, and S.Z. Qiao, Strategies for design of electrocatalysts for hydrogen evolution under alkaline conditions, *Mater. Today*, 36(2020), p. 125.

[2] J. Tang, M.S. Chu, F. Li, C. Feng, Z.G. Liu, and Y.S. Zhou, Development and progress on hydrogen metallurgy, *Int. J. Miner. Metall. Mater.*, 27(2020), No. 6, p. 713.

[3] N.T. Suen, S.F. Hung, Q. Quan, N. Zhang, Y.J. Xu, and H.M. Chen, Electrocatalysis for the oxygen evolution reaction: Recent development and future perspectives, *Chem. Soc. Rev.*, 46(2017), No. 2, p. 337.

[4] M. Wang, L. Zhang, Y.J. He, and H.W. Zhu, Recent advances in transition-metal-sulfide-based bifunctional electrocatalysts for overall water splitting, *J. Mater. Chem. A*, 9(2021), No. 9, p. 5320.

[5] K. Srinivas, Y.F. Chen, B. Wang, B. Yu, Y.J. Lu, Z. Su, W.L. Zhang, and D.X. Yang, Metal–organic framework-derived Fe-doped Ni_3Fe/$NiFe_2O_4$ heteronanoparticle-decorated carbon nanotube network as a highly efficient and durable bifunctional electrocatalyst, *ACS Appl. Mater. Interfaces*, 12(2020), No. 50, p. 55782.

[6] Z.L. Chen, H.L. Qing, R.R. Wang, and R.B. Wu, Charge pumping enabling Co–NC to outperform benchmark Pt catalyst for pH-universal hydrogen evolution reaction, *Energy Environ. Sci.*, 14(2021), No. 5, p. 3160.

[7] B. Liu, S. Wang, C.Y. Wang, B.Z. Ma, and Y.Q. Chen, Electrochemical behavior and corrosion resistance of IrO_2–ZrO_2 binary oxide coatings for promoting oxygen evolution in sulfuric acid solution, *Int. J. Miner. Metall. Mater.*, 27(2020), No. 2, p. 264.

[8] K. Srinivas, Y.J. Lu, Y.F. Chen, W.L. Zhang, and D.X. Yang, $FeNi_3$–Fe_3O_4 heterogeneous nanoparticles anchored on 2D MOF nanosheets/1D CNT matrix as highly efficient bifunctional electrocatalysts for water splitting, *ACS Sustainable Chem. Eng.*, 8(2020), No. 9, p. 3820.

[9] Z.F. Huang, S.B. Xi, J.J. Song, S. Dou, X.G. Li, Y.H. Du, C.Z. Diao, Z.C.J. Xu, and X. Wang, Tuning of lattice oxygen reactivity and scaling relation to construct better oxygen evolution electrocatalyst, *Nat. Commun.*, 12(2021), art. No. 3992.

[10] L.H. Liu, N. Li, J.R. Han, K.L. Yao, and H.Y. Liang, Multicomponent transition metal phosphide for oxygen evolution, *Int. J. Miner. Metall. Mater.*, 29(2022), No. 3, p. 503.

[11] M. Karpuraranjith, Y.F. Chen, B. Wang, J. Ramkumar, D.X. Yang, K. Srinivas, W. Wang, W.L. Zhang, and R. Manigandan, Hierarchical ultrathin layered MoS_2@$NiFe_2O_4$ nanohybrids as a bifunctional catalyst for highly efficient oxygen evolution and organic pollutant degradation, *J. Colloid Interface Sci.*, 592(2021), p. 385.

[12] K. Srinivas, Y.F. Chen, X.Q. Wang, B. Wang, M. Karpuraranjith, W. Wang, Z. Su, W.L. Zhang, and D.X. Yang, Constructing Ni/NiS heteronanoparticle-embedded metal-organic framework-derived nanosheets for enhanced water-splitting catalysis, *ACS Sustain. Chem. Eng.*, 9(2021), No. 4, p. 1920.

[13] X. Chen, X.Q. Wang, X.J. Zhang, K. Srinivas, D.W. Liu, X.C. Zhao, H.S. Yu, B. Wang, W.L. Zhang, and Y.F. Chen, Vertical $Fe(OH)_3$/Ni_9S_8 nanoarrays electrodeposited on stainless steel as binder-free electrocatalyst for highly efficient and stable oxygen evolution reaction, *J. Mater. Sci.*, 56(2021), No. 34, p. 19144.

[14] B. Wang, Y.F. Chen, X.Q. Wang, J. Ramkumar, X.J. Zhang, B. Yu, D.X. Yang, M. Karpuraranjith, and W.L. Zhang, rGO wrapped trimetallic sulfide nanowires as an efficient bifunctional catalyst for electrocatalytic oxygen evolution and photocatalytic organic degradation, *J. Mater. Chem. A*, 8(2020), No. 27, p. 13558.

[15] F. Yu, H.Q. Zhou, Y.F. Huang, J.Y. Sun, F. Qin, J.M. Bao, W.A.. Goddard, S. Chen, and Z.F. Ren, High-performance bifunctional porous non-noble metal phosphide catalyst for overall water splitting, *Nat. Commun.*, 9(2018), p. 2551.

[16] Y. Xiao, Y. Pei, Y.F. Hu, R.G. Ma, D.Y. Wang, and J.C. Wang, Co_2P@P-doped 3D porous carbon for bifunctional oxygen electrocatalysis, *Acta Phys. Chim. Sin.*, 37(2021), No. 7, art. No. 2009051.

[17] J.Z. Huang, J.C. Han, T. Wu, K. Feng, T. Yao, X.J. Wang, S.W. Liu, J. Zhong, Z.H. Zhang, Y.M. Zhang, and B. Song, Boosting hydrogen transfer during Volmer reaction at oxides/metal nanocomposites for efficient alkaline hydrogen evolution, *ACS Energy Lett.*, 4(2019), No. 12, p. 3002.

[18] S. Anantharaj, S. Kundu, and S. Noda, "The Fe Effect": A review unveiling the critical roles of Fe in enhancing OER activity of Ni and Co based catalysts, *Nano Energy*, 80(2021), p. 105514.

[19] X.J. Zhang, Y.F. Chen, M.L. Chen, B. Yu, B. Wang, X.Q. Wang, W.L. Zhang, and D.X. Yang, MOF derived multi-metal oxides anchored N, P-doped carbon matrix as efficient and durable electrocatalyst for oxygen evolution reaction, *J. Colloid Interface Sci.*, 581(2021), p. 608.

[20] K. Sun, Y.Q. Zhao, J. Yin, J. Jin, H.W. Liu, and P.X. Xi, Surface modification of $NiCo_2O_4$ nanowires using organic ligands for overall water splitting, *Acta Phys. Chim. Sin.*, 38(2022), No. 6, pp. 2107005-2107005.

[21] J.F. Zhang, Y. Jiang, Y. Wang, C.P. Yu, J.W. Cui, J.J. Wu, X.

Shu, Y.Q. Qin, J. Sun, J. Yan, H.M. Zheng, Y. Zhang, and Y.C. Wu, Ultrathin carbon coated mesoporous Ni–$NiFe_2O_4$ nanosheet arrays for efficient overall water splitting, *Electrochim. Acta*, 321(2019), p. 134652.

[22] M. Wang, L. Zhang, J.L. Pan, M.R. Huang, and H.W. Zhu, A highly efficient Fe-doped Ni_3S_2 electrocatalyst for overall water splitting, *Nano Res.*, 14(2021), No. 12, p. 4740.

[23] H. Su, S.J. Song, S.S. Li, Y.Q. Gao, L. Ge, W.Y. Song, T.Y. Ma, and J. Liu, High-valent bimetal Ni_3S_2/Co_3S_4 induced by Cu doping for bifunctional electrocatalytic water splitting, *Appl. Catal. B Environ.*, 293(2021), art. No. 120225.

[24] R.Z. Zhang, Z.Q. Zhu, J.H. Lin, K.F. Zhang, N. Li, and C.J. Zhao, Hydrolysis assisted *in situ* growth of 3D hierarchical FeS/NiS/nickel foam electrode for overall water splitting, *Electrochim. Acta*, 332(2020), p. 135534.

[25] H.M. Sun, Z.H. Yan, F.M. Liu, W.C. Xu, F.Y. Cheng, and J. Chen, Self-supported transition-metal-based electrocatalysts for hydrogen and oxygen evolution, *Adv. Mater.*, 32(2020), No. 3, p. 1806326.

[26] H.N. Nong, L.J. Falling, A. Bergmann, M. Klingenhof, H.P. Tran, C. Spöri, R. Mom, J. Timoshenko, G. Zichittella, A. Knop-Gericke, S. Piccinin, J. Pérez-Ramírez, B.R. Cuenya, R. Schlögl, P. Strasser, D. Teschner, and T.E. Jones, Key role of chemistry versus bias in electrocatalytic oxygen evolution, *Nature*, 589(2021), p. 408.

[27] J.T. Li, D. Chu, H. Dong, D.R. Baker, and R.Z. Jiang, Boosted oxygen evolution reactivity by igniting double exchange interaction in spinel oxides, *J. Am. Chem. Soc.*, 142(2020), No. 1, p. 50.

[28] L. Lv, Y.X. Chang, X. Ao, Z.S. Li, J.G. Li, Y. Wu, X.Y. Xue, Y.L. Cao, G. Hong, and C.D. Wang, Interfacial electron transfer on heterostructured Ni_3Se_4/FeOOH endows highly efficient water oxidation in alkaline solutions, *Mater. Today Energy*, 17(2020), p. 100462.

[29] X.T. Yu, M.Y. Wang, X.Z. Gong, Z.C. Guo, Z. Wang, and S.Q. Jiao, Self-supporting porous CoP-based films with phase-separation structure for ultrastable overall water electrolysis at large current density, *Adv. Energy Mater.*, 8(2018), No. 34, p. 1802445.

[30] C. Andronescu, S. Barwe, E. Ventosa, J. Masa, E. Vasile, B. Konkena, S. Möller, and W. Schuhmann, Powder catalyst fixation for post-electrolysis structural characterization of NiFe layered double hydroxide based oxygen evolution reaction electrocatalysts, *Angew. Chem. Int. Ed.*, 56(2017), No. 37, p. 11258.

[31] T.Z. Wu, X. Ren, Y.M. Sun, S.N. Sun, G.Y. Xian, G.G. Scherer, A.C. Fisher, D. Mandler, J.W. Ager, A. Grimaud, J.L. Wang, C.M. Shen, H.T. Yang, J. Gracia, H.J. Gao, and Z.J. Xu, Spin pinning effect to reconstructed oxyhydroxide layer on ferromagnetic oxides for enhanced water oxidation, *Nat. Commun.*, 12(2021), No. 1, p. 3634.

[32] Y.F. Zhao, H. Zhou, X.R. Zhu, Y.T. Qu, C. Xiong, Z.G. Xue, Q.W. Zhang, X.K. Liu, F.Y. Zhou, X.M. Mou, W.Y. Wang, M. Chen, Y. Xiong, X.G. Lin, Y. Lin, W.X. Chen, H.J. Wang, Z. Jiang, L.R. Zheng, T. Yao, J.C. Dong, S.Q. Wei, W.X. Huang, L. Gu, J. Luo, Y.F. Li, and Y.E. Wu, Simultaneous oxidative and reductive reactions in one system by atomic design, *Nat. Catal.*, 4(2021), No. 2, p. 134.

[33] S. Park, K. Jin, H.K. Lim, J. Kim, K.H. Cho, S. Choi, H. Seo, M.Y. Lee, Y.H. Lee, S. Yoon, M. Kim, H. Kim, S.H. Kim, and K.T. Nam, Spectroscopic capture of a low-spin Mn(IV)-oxo species in Ni–Mn_3O_4 nanoparticles during water oxidation catalysis, *Nat. Commun.*, 11(2020), No. 1, p. 5230.

[34] S.F. Zai, X.Y. Gao, C.C. Yang, and Q. Jiang, Ce-modified $Ni(OH)_2$ nanoflowers supported on $NiSe_2$ octahedra nanoparticles as high-efficient oxygen evolution electrocatalyst, *Adv. Energy Mater.*, 11(2021), No. 28, art. No. 2101266.

[35] L. Trotochaud, S.L. Young, J.K. Ranney, and S.W. Boettcher, Nickel–iron oxyhydroxide oxygen-evolution electrocatalysts: The role of intentional and incidental iron incorporation, *J. Am. Chem. Soc.*, 136(2014), No. 18, p. 6744.

[36] B.H. Park, M. Kim, N.K. Park, H.J. Ryu, J.I. Baek, and M. Kang, Single layered hollow NiO–NiS catalyst with large specific surface area and highly efficient visible-light-driven carbon dioxide conversion, *Chemosphere*, 280(2021), p. 130759.

[37] G.Y. Zhou, Y. Chen, H. Dong, L. Xu, X.E. Liu, C.W. Ge, D.M. Sun, and Y.W. Tang, Ultrafine monodisperse NiS/NiS_2 heteronanoparticles *in situ* grown on N-doped graphene nanosheets with enhanced electrocatalytic activity for hydrogen evolution reaction, *Int. J. Hydrog. Energy*, 44(2019), No. 48, p. 26338.

[38] L.A. Marusak and L.N. Mulay, Mössbauer and magnetic study of the antiferro to ferrimagnetic phase transition in Fe_9S_{10} and the magnetokinetics of the diffusion of iron atoms during the transition, *J. Appl. Phys.*, 50(1979), No. B3, p. 1865.

[39] Z.Y. Wang, J.T. Li, X.C. Tian, X.P. Wang, Y. Yu, K.A. Owusu, L. He, and L.Q. Mai, Porous nickel–iron selenide nanosheets as highly efficient electrocatalysts for oxygen evolution reaction, *ACS Appl. Mater. Interfaces*, 8(2016), No. 30, p. 19386.

[40] H.W. Nesbitt, D. Legrand, and G.M. Bancroft, Interpretation of Ni_2p XPS spectra of Ni conductors and Ni insulators, *Phys. Chem. Miner.*, 27(2000), No. 5, p. 357.

[41] X.R. Zheng, X.P. Han, Y.Q. Zhang, J.H. Wang, C. Zhong, Y.D. Deng, and W.B. Hu, Controllable synthesis of nickel sulfide nanocatalysts and their phase-dependent performance for overall water splitting, *Nanoscale*, 11(2019), No. 12, p. 5646.

[42] Y.J. Li, H.C. Zhang, M. Jiang, Q. Zhang, P.L. He, and X.M. Sun, 3D self-supported Fe-doped Ni_2P nanosheet arrays as bifunctional catalysts for overall water splitting, *Adv. Funct. Mater.*, 27(2017), No. 37, art. No. 1702513.

[43] I. Uhlig, R. Szargan, H.W. Nesbitt, and K. Laajalehto, Surface states and reactivity of pyrite and marcasite, *Appl. Surf. Sci.*, 179(2001), No. 1-4, p. 222.

[44] T. Dickinson, A.F. Povey, and P.M.A. Sherwood, Dissolution and passivation of nickel. an X-ray photoelectron spectroscopic study, *J. Chem. Soc., Faraday Trans. 1*, 73(1977), p. 327.

[45] S.Q. Zhao, S.J. Guo, C. Zhu, J. Gao, H. Li, H. Huang, Y. Liu, and Z.H. Kang, Achieving electroreduction of CO_2 to CH_3OH with high selectivity using a pyrite–nickel sulfide nanocomposite, *RSC Adv.*, 7(2017), No. 3, p. 1376.

[46] Y. Tang, C.H. Yang, Y.W. Yang, X.T. Yin, W.X. Que, and J.F. Zhu, Three dimensional hierarchical network structure of S–$NiFe_2O_4$ modified few-layer titanium carbides (MXene) flakes on nickel foam as a high efficient electrocatalyst for oxygen evolution, *Electrochim. Acta*, 296(2019), p. 762.

[47] G.X. Zhuang, Y.W. Chen, Z.Y. Zhuang, Y. Yu, and J.G. Yu, Oxygen vacancies in metal oxides: Recent progress towards advanced catalyst design, *Sci. China Mater.*, 63(2020), No. 11, p. 2089.

[48] D.X. Yang, Z. Su, Y.F. Chen, K. Srinivas, X.J. Zhang, W.L. Zhang, and H.P. Lin, Self-reconstruction of a MOF-derived chromium-doped nickel disulfide in electrocatalytic water oxidation, *Chem. Eng. J.*, 430(2022), art. No. 133046.

[49] K. Song, W.T. Li, R. Yang, Y.J. Zheng, X.S. Chen, X. Wang, G.L. Chen, and W.C. Lv, Controlled preparation of $Ni(OH)_2$/NiS nanosheet heterostructure as hybrid supercapacitor electrodes for high electrochemical performance, *Electrochim. Acta*, 388(2021), p. 138663.

[50] D.X. Yang, Z. Su, Y.F. Chen, Y.J. Lu, B. Yu, K. Srinivas, B. Wang, and W.L. Zhang, Double-shelled hollow bimetallic phosphide nanospheres anchored on nitrogen-doped graphene for boosting water electrolysis, *J. Mater. Chem. A*, 8(2020), No. 42, p. 22222.

[51] O. Diaz-Morales, I. Ledezma-Yanez, M.T.M. Koper, and F. Calle-Vallejo, Guidelines for the rational design of Ni-based double hydroxide electrocatalysts for the oxygen evolution re-

action, *ACS Catal.*, 5(2015), No. 9, p. 5380.
[52] M.Y. Wang, X.T. Yu, Z. Wang, X.Z. Gong, Z.C. Guo, and L. Dai, Hierarchically 3D porous films electrochemically constructed on gas–liquid–solid three-phase interface for energy application, *J. Mater. Chem. A*, 5(2017), No. 20, p. 9488.
[53] S. Intikhab, J.D. Snyder, and M.H. Tang, Adsorbed hydroxide does not participate in the Volmer step of alkaline hydrogen electrocatalysis, *ACS Catal.*, 7(2017), No. 12, p. 8314.
[54] B. Dong, X. Zhao, G.Q. Han, X. Li, X. Shang, Y.R. Liu, W.H. Hu, Y.M. Chai, H. Zhao, and C.G. Liu, Two-step synthesis of binary Ni–Fe sulfides supported on nickel foam as highly efficient electrocatalysts for the oxygen evolution reaction, *J. Mater. Chem. A*, 4(2016), No. 35, p. 13499.
[55] G. Liu, K.F. Wang, X.S. Gao, D.Y. He, and J.P. Li, Fabrication of mesoporous $NiFe_2O_4$ nanorods as efficient oxygen evolution catalyst for water splitting, *Electrochim. Acta*, 211(2016), p. 871.
[56] X. Shi, Y.F. Li, S.L. Bernasek, and A. Selloni, Structure of the $NiFe_2O_4$(001) surface in contact with gaseous O_2 and water vapor, *Surf. Sci.*, 640(2015), p. 73.
[57] S.H. Ahn, I. Choi, H.Y. Park, S.J. Hwang, S.J. Yoo, E. Cho, H.J. Kim, D. Henkensmeier, S.W. Nam, S.K. Kim, and J.H. Jang, Effect of morphology of electrodeposited Ni catalysts on the behavior of bubbles generated during the oxygen evolution reaction in alkaline water electrolysis, *Chem. Commun.*, 49(2013), No. 81, p. 9323.
[58] N. Mahmood, Y.D. Yao, J.W. Zhang, L. Pan, X.W. Zhang, and J.J. Zou, Electrocatalysts for hydrogen evolution in alkaline electrolytes: Mechanisms, challenges, and prospective solutions, *Adv. Sci.*, 5(2018), No. 2, p. 1700464.
[59] Y. Zheng, Y. Jiao, A. Vasileff, and S.Z. Qiao, The hydrogen evolution reaction in alkaline solution: From theory, single crystal models, to practical electrocatalysts, *Angew. Chem. Int. Ed.*, 57(2018), No. 26, p. 7568.